



## Topotactic Growth of Edge-Terminated MoS<sub>2</sub> from MoO<sub>2</sub> Nanocrystals

Dahl-Petersen, Christian; Sarić, Manuel; Brorson, Michael; Moses, Poul Georg; Rossmeisl, Jan; Lauritsen, Jeppe Vang; Helveg, Stig

*Published in:*  
A C S Nano

*Link to article, DOI:*  
[10.1021/acsnano.8b00125](https://doi.org/10.1021/acsnano.8b00125)

*Publication date:*  
2018

*Document Version*  
Peer reviewed version

[Link back to DTU Orbit](#)

### *Citation (APA):*

Dahl-Petersen, C., Sarić, M., Brorson, M., Moses, P. G., Rossmeisl, J., Lauritsen, J. V., & Helveg, S. (2018). Topotactic Growth of Edge-Terminated MoS<sub>2</sub> from MoO<sub>2</sub> Nanocrystals. *A C S Nano*, 12(6), 5351-5358. <https://doi.org/10.1021/acsnano.8b00125>

---

### General rights

Copyright and moral rights for the publications made accessible in the public portal are retained by the authors and/or other copyright owners and it is a condition of accessing publications that users recognise and abide by the legal requirements associated with these rights.

- Users may download and print one copy of any publication from the public portal for the purpose of private study or research.
- You may not further distribute the material or use it for any profit-making activity or commercial gain
- You may freely distribute the URL identifying the publication in the public portal

If you believe that this document breaches copyright please contact us providing details, and we will remove access to the work immediately and investigate your claim.

## Topotactic Growth of Edge-Terminated MoS from MoO Nanocrystals

Christian Dahl-Petersen, Manuel Sari#, Michael Brorson, Poul Georg Moses, Jan Rossmesl, Jeppe V. Lauritsen, and Stig Helveg

ACS Nano, Just Accepted Manuscript • DOI: 10.1021/acsnano.8b00125 • Publication Date (Web): 16 May 2018

Downloaded from <http://pubs.acs.org> on May 22, 2018

### Just Accepted

“Just Accepted” manuscripts have been peer-reviewed and accepted for publication. They are posted online prior to technical editing, formatting for publication and author proofing. The American Chemical Society provides “Just Accepted” as a service to the research community to expedite the dissemination of scientific material as soon as possible after acceptance. “Just Accepted” manuscripts appear in full in PDF format accompanied by an HTML abstract. “Just Accepted” manuscripts have been fully peer reviewed, but should not be considered the official version of record. They are citable by the Digital Object Identifier (DOI®). “Just Accepted” is an optional service offered to authors. Therefore, the “Just Accepted” Web site may not include all articles that will be published in the journal. After a manuscript is technically edited and formatted, it will be removed from the “Just Accepted” Web site and published as an ASAP article. Note that technical editing may introduce minor changes to the manuscript text and/or graphics which could affect content, and all legal disclaimers and ethical guidelines that apply to the journal pertain. ACS cannot be held responsible for errors or consequences arising from the use of information contained in these “Just Accepted” manuscripts.



# Topotactic Growth of Edge-Terminated MoS<sub>2</sub> from MoO<sub>2</sub> Nanocrystals

Christian Dahl-Petersen<sup>1,2</sup>, Manuel Sarić<sup>3</sup>, Michael Brorson<sup>1</sup>, Poul Georg Moses<sup>1</sup>, Jan Rossmeisl<sup>4</sup>, Jeppe Vang Lauritsen<sup>2</sup>, Stig Helveg<sup>1,\*</sup>

<sup>1</sup> Haldor Topsoe A/S, Haldor Topsøes Allé 1, DK-2800 Kgs. Lyngby, Denmark

<sup>2</sup> Interdisciplinary Nanoscience Center (iNANO), Aarhus University, Gustav Wieds Vej 14, DK-8000 Aarhus C, Denmark

<sup>3</sup> Technical University of Denmark, Department of Physics, DK-2800 Kgs. Lyngby, Denmark

<sup>4</sup> University of Copenhagen, Nano-Science Center, Department of Chemistry, Universitetsparken 5, DK-2100 Copenhagen, Denmark

\*Address correspondence to [sth@topsoe.com](mailto:sth@topsoe.com)

**Keywords.** Topotaxy, growth mechanism, MoS<sub>2</sub>, edge-termination, *in situ* transmission electron microscopy, density functional theory

## Abstract.

Layered transition metal dichalcogenides have distinct physicochemical properties at their edge-terminations. The production of an abundant density of edge structures is, however, impeded by

1  
2  
3 the excess surface energy of edges compared to basal planes and would benefit from insight into  
4 the atomic growth mechanisms. Here, we show that edge-terminated MoS<sub>2</sub> nanostructures can  
5 form during sulfidation of MoO<sub>2</sub> nanocrystals by using *in situ* transmission electron microscopy  
6 (TEM). Time-resolved TEM image series reveal that the MoO<sub>2</sub> surface can sulfide by inward  
7 progression of MoO<sub>2</sub>(20-2):MoS<sub>2</sub>(002) interfaces resulting in upright-oriented and edge-  
8 exposing MoS<sub>2</sub> sheets. This topotactic growth is rationalized in interplay with density functional  
9 theory calculations by successive O-S exchange and Mo sublattice restructuring steps. The  
10 analysis shows that *e*-MoS<sub>2</sub> formation is energetically favorable at MoO<sub>2</sub>(110) surfaces and  
11 provides a necessary requirement for the propensity of a specific MoO<sub>2</sub> surface termination to  
12 form edge-terminated MoS<sub>2</sub>. Thus, the present findings should benefit the rational development  
13 of transition metal dichalcogenide nanomaterials with abundant edge-terminations.  
14  
15  
16  
17  
18  
19  
20  
21  
22  
23  
24  
25  
26  
27  
28  
29

30  
31 Progress in the synthesis of layered transition metal dichalcogenides (TMDCs) has led to a  
32 variety of nanoscale structures including fullerenes, tubes/wires and platelets, each with distinct  
33 physicochemical properties.<sup>1</sup> These TMDC structures are derived from layers of hexagonally  
34 arranged transition metal atoms (*e.g.* Mo and W) in which each metal atom is coordinated by six  
35 chalcogenide atoms usually in a trigonal prismatic geometry. Such TMDC sheets are terminated  
36 by extended basal planes with a regular atomic arrangement and by atomically thin edges. Due to  
37 the reduced atomic coordination, the edges expose structures that markedly differ from those of  
38 the basal plane and, in turn, offer distinct electronic,<sup>2,3</sup> optical,<sup>4</sup> magnetic<sup>5</sup> and chemical<sup>6,7</sup>  
39 properties. In particular, the edges of MoS<sub>2</sub> sheets have long received interest as catalysts for  
40 mineral oil refining,<sup>8,9</sup> hydrogen evolution,<sup>10,11</sup> CO<sub>2</sub> reduction<sup>12</sup> and photo-oxidation<sup>13</sup> reactions,  
41 whereas the unperturbed MoS<sub>2</sub> basal plane is regarded as essentially inert. These catalytic  
42  
43  
44  
45  
46  
47  
48  
49  
50  
51  
52  
53  
54  
55  
56  
57  
58  
59  
60

1  
2  
3 processes would therefore benefit from edges that are more abundantly available. In addition,  
4 exposed edges are also beneficial for reducing steric hindrance in adsorption of *e.g.* heavy sulfur-  
5 containing organic compounds, which is a prime target in improving catalysts for oil refining  
6 processes.<sup>14</sup>  
7  
8  
9  
10

11  
12 The availability of edge sites depends on the size, shape and orientation of the TMDC  
13 sheets. As the edge terminations are associated with a considerably higher surface energy than  
14 the basal plane, the formation of edge sites is suppressed compared to the growth of basal planes.  
15 Hence, TMDC sheets are expected to form with extended basal plane exposed to the  
16 surroundings and oriented parallel with a supporting surface. In contrast, the sulfidation or  
17 thermolysis of molybdenum precursors dispersed on a support material have empirically been  
18 found to also produce upright-oriented and thereby edge-exposing MoS<sub>2</sub> sheets.<sup>12,13,15-26</sup>  
19 Common for the majority of these edge-favoring synthesis procedures is the employment of a  
20 dense molybdenum precursor in the form of nanoparticles or thin films.<sup>12,13,15,18-23</sup> The  
21 appearance of the upright orientation has been attributed to a strong bonding of the MoS<sub>2</sub> edge to  
22 the supporting material to counteract the thermodynamic drive towards a parallel  
23 orientation.<sup>16,27,28</sup> However, an elaborate understanding of the atomic mechanisms governing the  
24 formation of the edge-terminated MoS<sub>2</sub> is still lacking and bottom-up strategies have therefore  
25 not been available for synthesizing edge-terminated materials with superior catalytic and other  
26 functionalities.  
27  
28  
29  
30  
31  
32  
33  
34  
35  
36  
37  
38  
39  
40  
41  
42  
43  
44  
45

46  
47 With recent advances in transmission electron microscopy (TEM), dynamic  
48 transformations of solid materials can now be monitored *in situ* at high spatial resolution during  
49 exposure to reactive gas or liquid environments. By acquiring time-lapsed series of TEM images,  
50 it has become possible to gain insight into the mechanisms and kinetics involved in the formation  
51  
52  
53  
54  
55  
56  
57  
58  
59  
60

1  
2  
3 of different types of nanometer-sized structures.<sup>29-31</sup> Here, we employ this TEM approach to  
4 monitor the growth of MoS<sub>2</sub> nanostructures from molybdenum(IV) oxide (MoO<sub>2</sub>) nanocrystals *in*  
5 *situ* during exposure to a reactive H<sub>2</sub>S/H<sub>2</sub> atmosphere. The time-resolved TEM image series  
6 reveal that the oxide nanocrystal surfaces can form domains of upright-oriented MoS<sub>2</sub> sheets by  
7 the progression of the MoO<sub>2</sub>(20-2):MoS<sub>2</sub>(002) interface from the MoO<sub>2</sub> surface toward its bulk,  
8 in addition to domains of parallel-oriented MoS<sub>2</sub> sheets (Figure 1a). This topotactical reaction is  
9 explained in interplay with density functional theory (DFT) modelling by repeated steps of O-S  
10 exchange and Mo sublattice restructuring. Specifically, these reaction steps exhibit a marked  
11 dependency of the MoO<sub>2</sub> surface structure in the way that energetically favors formation of edge-  
12 terminated MoS<sub>2</sub> sheets at the MoO<sub>2</sub>(110) surface. The implication of these findings is therefore  
13 that (110)-terminated MoO<sub>2</sub> precursors can produce abundantly available MoS<sub>2</sub> edge sites and  
14 that the reaction steps offer descriptors for surface topotaxy, which should, in general, facilitate  
15 the design of TMDC nanomaterials with superior edge functionalities.

## 35 Results/Discussion

36  
37 The electron microscope experiments used MoO<sub>2</sub> nanoparticles as precursor because (1)  
38 previous studies suggested that molybdenum-dense precursors favor formation of upright-  
39 oriented MoS<sub>2</sub> sheets, (2) nanoparticles enable surface-profile imaging by electron microscopy  
40 and (3) reduced MoO<sub>3</sub>, such as MoO<sub>2</sub> and MoO<sub>3-x</sub>, has been considered as intermediate in  
41 sulfidation by H<sub>2</sub>S/H<sub>2</sub> into inorganic fullerene structures.<sup>32,33</sup> The molybdenum(IV) oxide  
42 precursor was formed by heating ammonium heptamolybdate tetrahydrate  
43 ((NH<sub>4</sub>)<sub>6</sub>[Mo<sub>7</sub>O<sub>24</sub>]·4H<sub>2</sub>O) to 450°C at the base vacuum of ca. 5×10<sup>-6</sup> mbar (Methods). The  
44 procedure resulted in nanoparticles with projected diameters in the range of 5 to 20 nm and with  
45  
46  
47  
48  
49  
50  
51  
52  
53  
54  
55  
56  
57  
58  
59  
60

1  
2  
3 the monoclinic MoO<sub>2</sub> crystal structure<sup>34,35</sup> (Figures S1 and S2 in the Supporting Information).  
4  
5 The MoO<sub>2</sub> nanocrystals exposed predominantly low-indexed facets such as *e.g.* (100), (010) and  
6  
7 (110) (Figure S2 in the Supporting Information). Subsequently, the as-prepared MoO<sub>2</sub>  
8  
9 nanocrystals were exposed to a gas mixture of 10% H<sub>2</sub>S in H<sub>2</sub> at a total pressure of 1 mbar and  
10  
11 heated to a nominal temperature of 250-300°C for 240-300 min inside the electron microscope  
12  
13 (Methods). Such low temperatures have previously been associated with the synthesis of upright-  
14  
15 oriented MoS<sub>2</sub> sheets.<sup>16,17</sup> During the present treatment, structures emerged that are attributed to  
16  
17 molybdenum sulfide because they were absent in similar experiments without H<sub>2</sub>S in the reaction  
18  
19 gas (Figure S3 in the Supporting Information). The molybdenum sulfide structures appeared with  
20  
21 two distinctly different orientations relative to the surface of the MoO<sub>2</sub> nanocrystals.  
22  
23  
24  
25

26 The first structure, denoted *e*-MoS<sub>2</sub>, represents our main finding and surprisingly consists  
27  
28 of sheets oriented upright with respect to the projected nanocrystal surface (Figure 1a). The  
29  
30 sheets represent lattice fringes with spacing of ca. 0.62 nm, corresponding to the MoS<sub>2</sub> (002)  
31  
32 lattice planes (Figure 1b). Domains of *e*-MoS<sub>2</sub> extend from the projected periphery towards the  
33  
34 bulk of the nanocrystal and typically consist of 3-8 MoS<sub>2</sub> sheets with length of 1 - 5 nm (Figure  
35  
36 1b and Figures S4-S6 in the Supporting Information). Thus, *e*-MoS<sub>2</sub> exposes predominantly edge  
37  
38 sites to the surroundings. Due to the projection geometry, it is possible that the *e*-MoS<sub>2</sub> only  
39  
40 partly covers the corresponding surface termination oriented along the electron beam direction  
41  
42 (Figure 2) and that the remaining MoO<sub>x</sub> sites eventually sulfide to cover the nanocrystal surface  
43  
44 by *p*-MoS<sub>2</sub>. Moreover, the anisotropy of MoS<sub>2</sub> sheets implies that the corresponding TEM image  
45  
46 contrast depends strongly on their orientation. MoS<sub>2</sub> sheets oriented with their (002) basal plane  
47  
48 along the electron beam direction obtain strong phase contrast in high-resolution TEM images,  
49  
50 whereas MoS<sub>2</sub> sheets having the (002) planes tilted more than ca. 9° off the electron beam  
51  
52  
53  
54  
55  
56  
57  
58  
59  
60

1  
2  
3 direction appear with a markedly diminished contrast due to the reduced number of atoms  
4 contributing to the projected electrostatic potential.<sup>36,37</sup> Therefore, domains of *e*-MoS<sub>2</sub> may be  
5 present in other parts of the MoO<sub>2</sub> nanocrystal and remain unresolved in the TEM images due to  
6 their orientation. It is therefore not surprising that the *e*-MoS<sub>2</sub> structure was observed in only  
7 about 13% of all nanocrystals (Note in the Supporting Information). However, the low  
8 abundance of *e*-MoS<sub>2</sub> could also reflect that only certain surface facets of the parent MoO<sub>2</sub>  
9 nanocrystal promote growth of the edge-terminated MoS<sub>2</sub>.  
10  
11  
12  
13  
14  
15  
16  
17  
18

19 The second structure, denoted *p*-MoS<sub>2</sub>, consists of sheets contouring the surface of most  
20 of the MoO<sub>2</sub> nanocrystals (Figure 1a, note in the Supporting Information). Occasionally, these  
21 sheets stack with an interlayer spacing of ca. 0.63 nm, corresponding to the MoS<sub>2</sub>(002) lattice  
22 planes, and reveal internal lattice fringes with spacing of 0.27 nm, corresponding to (100) lattice  
23 planes (Figure 1b and 1c). The *p*-MoS<sub>2</sub> sheets extend along the projected MoO<sub>2</sub> surface parallel  
24 to the electron beam. In addition, the sheets are likely also contouring those parts of the MoO<sub>2</sub>  
25 nanocrystal surface that is *not* parallel with the electron beam direction (within  $\sim\pm 9^\circ$ ) and *p*-  
26 MoS<sub>2</sub> therefore remain undetectable in such regions of the TEM images due to their orientation  
27 and overlaid contrast from the projected bulk MoO<sub>2</sub> nanocrystal. Thus, the *p*-MoS<sub>2</sub> structure  
28 consists of MoS<sub>2</sub> sheets that are confined to the surface region of the MoO<sub>2</sub> nanocrystal and  
29 expose predominantly the MoS<sub>2</sub>(002) basal plane, similarly to previous findings for fullerene  
30 MoS<sub>2</sub> structures.<sup>32,33,38</sup>  
31  
32  
33  
34  
35  
36  
37  
38  
39  
40  
41  
42  
43  
44  
45  
46

47 To address the growth mode of the edge-terminated MoS<sub>2</sub>, *e*-MoS<sub>2</sub>, an analysis is first  
48 presented of time-resolved series of TEM images that were acquired of individual MoO<sub>2</sub>  
49 nanocrystals as the sulfidation reaction progressed. Figure 2 shows an image sequence (extracted  
50 from Video S1 in the Supporting Information) revealing the dynamic transformation of the  
51  
52  
53  
54  
55  
56  
57  
58  
59  
60



1  
2  
3 surface on a MoO<sub>2</sub> nanocrystal during sulfidation. The images show that the MoS<sub>2</sub> sheets  
4 nucleate directly in the exposed MoO<sub>2</sub> surface without any additional surface layers. Adjacent  
5 MoS<sub>2</sub> sheets form simultaneously and establish a domain of *e*-MoS<sub>2</sub>. Subsequently, the MoS<sub>2</sub>  
6 sheets grow in length from the original surface toward the bulk of the MoO<sub>2</sub> nanocrystal,  
7 reaching a final length of ca. 2.8 nm. Figure S7 in the Supporting Information shows that the  
8 MoS<sub>2</sub> sheets grow initially fast and that the growth stagnates at longer sulfidation times. The  
9 decay of the growth rate may be due to the slower mass transport through the bulk of the  
10 nanoparticle. Similar dynamic behavior is revealed in the formation of shorter *e*-MoS<sub>2</sub> structures  
11 albeit at a corresponding lower signal-to-noise ratio (Figure S5 in the Supporting Information).  
12 On average, *e*-MoS<sub>2</sub> sheets observed *in situ* grew to a final average projected length of 1.7 nm  
13 (with a standard deviation of 0.6 nm) and sheets observed *post mortem* had grown to an average  
14 projected length of 1.8 nm (with a standard deviation of 0.7 nm) (Figure S8 in the Supporting  
15 Information). This conformity demonstrates that alterations of the growth process induced by the  
16 electron illumination were insignificant with the applied low dose-rate imaging protocol and that  
17 the observed MoS<sub>2</sub> formation is inherent to the sulfidation reaction as such (Methods). Thus, the  
18 time-resolved observations indicate that growth of *e*-MoS<sub>2</sub> proceeded by an O-S exchange  
19 reaction and by an inward progression of the MoO<sub>2</sub>:MoS<sub>2</sub> interface from the surface of the MoO<sub>2</sub>  
20 nanocrystal upon continued exposure to the sulfur-rich gas.  
21  
22  
23  
24  
25  
26  
27  
28  
29  
30  
31  
32  
33  
34  
35  
36  
37  
38  
39  
40  
41  
42  
43

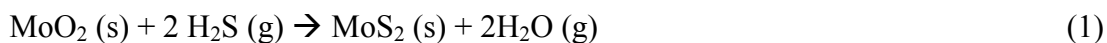
44 To address the relation between the *e*-MoS<sub>2</sub> and MoO<sub>2</sub> host nanocrystal structures, their  
45 interface is examined at the atomic-scale. Figure 3 shows a close-up TEM image of the interface,  
46 which reveals a threefold periodicity with three MoO<sub>2</sub>(20-2) lattice planes matching one single  
47 MoS<sub>2</sub>(002) lattice plane. The lattice matching at the interface influenced the MoS<sub>2</sub> interlayer  
48 spacing in such a way that the spacing varied with the distance from the MoO<sub>2</sub>:MoS<sub>2</sub> interface to  
49  
50  
51  
52  
53  
54  
55  
56  
57  
58  
59  
60

1  
2  
3 the nanocrystal surface. Specifically, the MoS<sub>2</sub>(002) lattice spacing was larger closer to the  
4 interface, corresponding to  $3a_{\text{MoO}_2[20-2]} = 0.73$  nm, and smaller near the nanocrystal surface,  
5  
6 corresponding to  $a_{\text{MoS}_2[002]} = 0.62$  nm (Figure 3). Consistently, shorter *e*-MoS<sub>2</sub> slabs were  
7  
8 separated by ca. 0.73 nm (Figures S4 and S6 in the Supporting Information). The larger  
9  
10 MoS<sub>2</sub>(002) lattice spacing near the interface constitutes a geometric strain of +17%, which is  
11  
12 energetically feasible due to the weak van der Waals interaction between the MoS<sub>2</sub> sheets. A  
13  
14 similar analysis of the crystal lattice planes in high-resolution TEM images of nine additional  
15  
16 MoO<sub>2</sub> nanocrystals also characterized the interface as MoO<sub>2</sub>(20-2):MoS<sub>2</sub>(002) (Figure S4 in the  
17  
18 Supporting Information). This interfacial relation of the two crystal lattices shows that the *e*-  
19  
20 MoS<sub>2</sub> sheets formed as the result of a topotactic transformation of the MoO<sub>2</sub> surface region.<sup>39</sup>  
21  
22 Moreover, as the MoS<sub>2</sub> sheets are oriented upright with respect to the projected MoO<sub>2</sub> surface, *e*-  
23  
24 MoS<sub>2</sub> must nucleate at surface facets inclined from the MoO<sub>2</sub>(20-2) lattice planes, including the  
25  
26 more abundant low-indexed surface terminations, such as (110), (010) and (100).  
27  
28  
29  
30  
31  
32

33 Furthermore, the conversion of MoO<sub>2</sub> into MoS<sub>2</sub> by anion exchange also entails a  
34  
35 restructuring of the Mo sublattice due to different Mo atom densities. MoO<sub>2</sub> is a monoclinic  
36  
37 structure with a density of 30.4 Mo atoms/nm<sup>3</sup>, and MoS<sub>2</sub> is a hexagonal structure with a density  
38  
39 of 18.8 Mo atoms/nm<sup>3</sup>. The corresponding volume expansion of 62% per Mo atom implies that  
40  
41 Mo atoms were expelled from the bulk MoO<sub>2</sub> during formation of *e*-MoS<sub>2</sub>. These Mo atoms  
42  
43 possibly contributed to *p*-MoS<sub>2</sub>, because *p*-MoS<sub>2</sub> and *e*-MoS<sub>2</sub> formed simultaneously (Figure 2)  
44  
45 and *p*-MoS<sub>2</sub> formed at the exterior surface of the MoO<sub>2</sub> nanocrystals, causing an apparent  
46  
47 increase in the projected size of the nanocrystals (Figure S9 in the Supporting Information).  
48  
49  
50

51 The present observations of topotactic growth of edge-terminated MoS<sub>2</sub> sheets from  
52  
53 MoO<sub>2</sub> can be rationalized by the atomistic mechanism proposed in Figure 4. The consistency of  
54  
55  
56  
57  
58  
59  
60

1  
2  
3 this mechanism is examined by means of DFT calculations, combined with a thermodynamic  
4 extrapolation to the present sulfidation conditions (Methods). First, the conversion of bulk MoO<sub>2</sub>  
5 to MoS<sub>2</sub> is addressed by the reaction:  
6  
7



8  
9  
10  
11 For this reaction, a calculation shows a Gibbs free energy change of -1.00 eV, corresponding to  
12 an average gain of -0.50 eV/S atom, with 0.9 mbar H<sub>2</sub> and 0.1 mbar H<sub>2</sub>S at 250 °C. The  
13 sulfidation described by eq. (1) initiates at the MoO<sub>2</sub> surface.<sup>40,41</sup> The surface sulfidation by H<sub>2</sub>S  
14 is modelled at the low-indexed (110), (010) or (100) facets of MoO<sub>2</sub>, consistent with the TEM  
15 observations. This process is associated with a free energy change of -0.01 eV/S atom, -0.29  
16 eV/S atom and +0.09 eV/S atom for the MoO<sub>2</sub> (110), (010) and (100) surfaces, respectively, at  
17 the same conditions. Thus, only the (110) and (010) surface terminations tend to sulfide (Figure  
18 S10 in the Supporting Information), whereas the (100) surface remains oxidic under the present  
19 reaction conditions.  
20  
21  
22  
23  
24  
25  
26  
27  
28  
29  
30  
31

32  
33 Following the initial sulfidation, the MoO<sub>2</sub> surface is envisioned to develop by successive  
34 steps of Mo sublattice reconstruction and O-S exchange to accommodate the upright oriented  
35 MoS<sub>2</sub> sheets. At the sulfided MoO<sub>2</sub>(110) surface, every second topmost [-11-1]-row contains half  
36 the number of Mo atoms (row 1 and 3 in Figure 4a) compared to the [-11-1]-rows in the bulk  
37 MoO<sub>2</sub> structure (row 4 and 5 in Figure 4a). A stepwise displacement of these topmost [-11-1]-  
38 rows toward each other, by  $1a_{[20-2]}$  as outlined for row 1 (a → b in Figure 4) and row 3 (b → c in  
39 Figure 4), results in a sulfided row of Mo atoms with a density similar to MoS<sub>2</sub>[100] (note in the  
40 Supporting Information). Moreover, the repetition of the displacements along the MoO<sub>2</sub> surface  
41 develops a threefold periodicity of MoO<sub>2</sub>(20-2):MoS<sub>2</sub>(002) interface, in agreement with the TEM  
42 images. The [-11-1]-row displacements uncover underlying oxide [-11-1]-rows (row 2, 4 and 5  
43  
44  
45  
46  
47  
48  
49  
50  
51  
52  
53  
54  
55  
56  
57  
58  
59  
60

1  
2  
3 in Figure 4) comparable to the pristine oxide surface. As the exposure to the sulfiding  
4 environment is continuous in the experiments, these oxide rows likewise undergo O-S exchange  
5 as well. A two-row high  $\text{MoS}_2$  sheet therefore emerges extending one row in and out from the  
6 initial surface (row 1+3 and 2 in Figure 4c). Moreover, the deeper-lying  $\text{MoO}_2$  [-11-1]-rows also  
7 partly sulfide upon exposure to the reaction environment (row 4 and 5), and these rows may  
8 subsequently transform in a similar way as the outermost rows (row 1 and 3). That is, half of the  
9 sulfided Mo atoms in the [-11-1]-rows (row 4 and 5) are displaced into an additional sheet that  
10 extends the  $e\text{-MoS}_2$  sheet outwards. The remaining half-filled Mo [-11-1]-rows (row 4 and 5)  
11 mimic the initial state of the sulfided surface (Figure 4a) and therefore undergo the same  
12 transformations, resulting in a four-row  $e\text{-MoS}_2$  sheet (Figure 4d). As a result, the mechanism  
13 outlined in Figure 4 a-d becomes cyclic and, in turn, develops an  $e\text{-MoS}_2$  structure with a  
14  $\text{MoO}_2(20\text{-}2):\text{MoS}_2(002)$  interface and a threefold periodicity, consistent with the experimental  
15 observations. To corroborate this mechanism, the O-S exchange and Mo [-11-1]-row  
16 displacement steps were examined by DFT calculations to evaluate the Gibbs free energy for  
17 each state (Methods). Figure 4e shows a successive lowering of the Gibbs free energy per unit  
18 cell as the sulfidation reaction progressed, demonstrating that the proposed mechanism for the  
19 topotactic growth of  $e\text{-MoS}_2$  at the  $\text{MoO}_2(110)$  surface is plausible.

20  
21  
22  
23  
24  
25  
26  
27  
28  
29  
30  
31  
32  
33  
34  
35  
36  
37  
38  
39  
40  
41  
42 The mechanism in Figure 4 implies that the  $e\text{-MoS}_2$  sheets grow to the same extent  
43 inward and outward from the original  $\text{MoO}_2$  surface. In contrast, the  $\text{MoS}_2$  sheets are observed to  
44 progress mainly inward and only modestly outward from the original  $\text{MoO}_2$  surface in the  
45 experiment (Figure 2). The asymmetric growth of the  $e\text{-MoS}_2$  sheets possibly occurs under the  
46 experimental conditions, because the Mo atoms expelled from the  $\text{MoO}_2$  bulk are free to migrate  
47 to sites on the  $\text{MoO}_2$  surface where incorporation into  $p\text{-MoS}_2$  can occur. In contrast, in the DFT  
48  
49  
50  
51  
52  
53  
54  
55  
56  
57  
58  
59  
60

1  
2  
3 modelling the same Mo atoms are added as an outward extension of the MoS<sub>2</sub> layer, due to the  
4 geometrical constraint of the employed unit cell. The difference may reflect that, in the  
5 experimental situation, the outward growth is kinetically limited or the emergence of the basal  
6 plane of *p*-MoS<sub>2</sub> is energetically favored over *e*-MoS<sub>2</sub> sheets protruding outward from the  
7 original the MoO<sub>2</sub> surface.  
8  
9

10  
11  
12 To address the surface dependency of the topotactic reaction, the sulfidation mechanism  
13 is compared on the MoO<sub>2</sub> (110) and (010) surfaces (Figure 4 and Figure S11 in the Supporting  
14 Information). For both surfaces, the energy gain upon sulfidation is lower than the limit set by  
15 equation (1) for growth of bulk MoS<sub>2</sub> from MoO<sub>2</sub> (0.50 eV/S atom). Specifically, for the MoO<sub>2</sub>  
16 (110) and (010) surface, the corresponding Gibbs free energy difference from the surface to bulk  
17 sulfidation is -0.49 eV/S-atom (-0.50 eV/S atom minus -0.01 eV/S atom) and -0.21 eV/S atom (-  
18 0.50 eV/S atom minus -0.29 eV/S atom), respectively, under the present conditions. Thus, S  
19 atoms are less stable on the (110) than the (010) surface with respect to the *e*-MoS<sub>2</sub> structure. In  
20 addition, the Mo sublattice restructuring also exhibits a surface-dependency. Whereas  
21 displacement of the [-11-1] rows is spontaneous on the MoO<sub>2</sub>(110) surface (a → b in Figure 4e),  
22 the displacement of [101]-rows on the MoO<sub>2</sub>(010) surface into a one-row high MoS<sub>2</sub> sheet (a →  
23 b in Figure S11 in the Supporting Information) is associated with a Gibbs free energy change of  
24 +2.74 eV/unit-cell (Figure 4e). This energy change results from the higher Mo atom density in  
25 the (010) surface (note in the Supporting Information) and adds a barrier for restructuring the Mo  
26 sublattice that suppresses growth of *e*-MoS<sub>2</sub>. Thus, the calculations show that growth of *e*-MoS<sub>2</sub>  
27 is favored on MoO<sub>2</sub>(110) due to the large energy gain for transferring surface S atoms into bulk  
28 MoS<sub>2</sub> and the spontaneous and facile restructuring the Mo sublattice, whereas formation of *e*-  
29 MoS<sub>2</sub>  
30  
31  
32  
33  
34  
35  
36  
37  
38  
39  
40  
41  
42  
43  
44  
45  
46  
47  
48  
49  
50  
51  
52  
53  
54  
55  
56  
57  
58  
59  
60

1  
2  
3 MoS<sub>2</sub> is hindered on MoO<sub>2</sub>(010) due to the smaller energy gain in the S transfer and the larger  
4  
5 barrier for Mo sublattice restructuring.  
6  
7  
8  
9  
10

## 11 12 13 **Conclusion**

14  
15  
16 The present study demonstrates the O-S exchange energy and the Mo sublattice  
17 reconstruction energy as descriptors for the propensity of a specific MoO<sub>2</sub> surface to form *e*-  
18 MoS<sub>2</sub>, and the analysis provides a necessary requirement for a MoO<sub>2</sub> surface to facilitate a  
19 spontaneous topotactic transformation into edge-terminated MoS<sub>2</sub>. This insight may help  
20 understanding previous reports on oriented nucleation and growth of MoS<sub>2</sub> sheets based on the  
21 surface properties of the molybdenum oxide precursors.<sup>16-18</sup> Moreover, the present findings  
22 suggest that the *e*-MoS<sub>2</sub> growth is energetically favored at (110) surfaces of a MoO<sub>2</sub>  
23 nanomaterials under the present growth conditions. In the future, developing shape-selective  
24 synthesis procedures of MoO<sub>2</sub> nanomaterials with an enhanced abundance of (110) surface  
25 terminations therefore seems as one viable route for optimizing the abundance of *e*-MoS<sub>2</sub>. The *e*-  
26 MoS<sub>2</sub> formation could be kinetically limited by adsorption or diffusion processes not considered  
27 in the present analysis. Such limitations can be addressed by detailed characterization using  
28 oxygen adsorption of the MoS<sub>2</sub> edge sites<sup>42</sup> and a shape-determination of the MoO<sub>2</sub> nanomaterial  
29 using electron microscopy or X-ray diffraction.<sup>43</sup> Conceptually, the present descriptors of surface  
30 topotaxy may be generally applicable in guiding bottom-up synthesis procedures of TMDC  
31 nanomaterials towards enhanced edge-functionalities.  
32  
33  
34  
35  
36  
37  
38  
39  
40  
41  
42  
43  
44  
45  
46  
47  
48  
49  
50  
51  
52  
53  
54  
55  
56  
57  
58  
59  
60

## Methods/Experimental

**Sample preparation and sulfidation.** Ammonium heptamolybdate tetrahydrate,  $(\text{NH}_4)_6\text{Mo}_7\text{O}_{24}\cdot 4\text{H}_2\text{O}$  (Merck, 1180336, minimum 99% nominal purity) was used as molybdenum precursor. The precursor granulate was ground to a fine powder and dispersed in its dry state onto plasma-cleaned Protochips Aduro E-chips or FEI Company NanoEx chips. Precursor particles were approximately 2-5  $\mu\text{m}$  wide and overhung the membrane holes near the center of the chip membrane. Heating of the chips to 450°C in the microscope base vacuum transformed the precursor into  $\text{MoO}_2$  nanoparticles ranging from 5 to 20 nm in width. For the Aduro E-chips,  $\text{MoO}_2$  nanoparticles protruding from holes in the second innermost quadrant of 7x7 hole arrangement were examined in the electron microscope to ensure temperature uniformity<sup>44</sup> and to minimize the image contrast contribution from the chip membranes. The NanoEx chips have a uniform temperature across the perforated membrane,<sup>45</sup> and particles protruding from any hole were imaged by TEM.

To initiate the sulfidation reaction, the temperature of the chip was lowered to 300°C or 250°C, and subsequently a premixed gas with 10%  $\text{H}_2\text{S}$  in  $\text{H}_2$  (Air Liquide, nominal purity 98% for  $\text{H}_2\text{S}$  and 99.999% for  $\text{H}_2$ ) was introduced into the electron microscope at time = 0 min. The gas composition was continuously monitored using a quadrupole mass spectrometer (Balzers Prisma QMS 200) positioned at the microscope second differential pumping step for masses 2, 16, 18, 32, 33 and 34 AMU corresponding to signals from  $\text{H}_2$ ,  $\text{O}_2$ ,  $\text{H}_2\text{O}$ , S, HS, and  $\text{H}_2\text{S}$ . This showed that a constant gas composition was obtained after 5 min at constant gas pressure (Figure S12 in the Supporting Information). The ion currents were sampled at a total acquisition time of 11 sec.

1  
2  
3 **Transmission electron microscopy (TEM).** The growth of MoS<sub>2</sub> was examined by means of a  
4 Philips CM300 FEG-ST transmission electron microscope, which is equipped with a differential  
5 pumping system and heating stages to enable the exposure of solid specimens to reactive gasses  
6 and elevated temperatures.<sup>37,46</sup> Specifically, this microscope is dedicated to experiments  
7 including corrosive sulfur-containing gases.<sup>37</sup> The microscope was operated at a primary electron  
8 energy of 300 keV and with an electron dose-rate of 150 e<sup>-</sup>/(Å<sup>2</sup>s) for *in situ* observations with  
9 10% H<sub>2</sub>S in H<sub>2</sub> at 1 mbar total pressure in the sample region and of 200 e<sup>-</sup>/(Å<sup>2</sup>s) for *post mortem*  
10 observations under a high vacuum of better than 5x10<sup>-6</sup> mbar in the sample region. The applied  
11 gas environment reduced the electron transmittance by only ca. 3% relative to vacuum.  
12 Therefore, electron doses and dose-rates are quoted with reference to measurements in the  
13 evacuated microscope. Moreover, the microscope projection system was set at a magnification  
14 corresponding to an effective pixel size ranging from 0.03 nm to 0.07 nm of the charged coupled  
15 device (CCD) camera (Tietz F114) during TEM image acquisition. These magnification settings  
16 are sufficient to resolve the MoS<sub>2</sub> (100) lattice planes of spacing 0.27 nm and the MoO<sub>2</sub> (20-2)  
17 lattice planes of spacing 0.24 nm, as the shortest lattice spacings. Moreover, imaging was done at  
18 focus settings close to the Scherzer defocus value of  $f = -64$  nm to ensure a large contrast  
19 information transfer for the MoS<sub>2</sub> (002) and (100) lattice planes and the MoO<sub>2</sub> (20-2) lattice  
20 planes. The CCD illumination time was 0.5 - 1 s per image.  
21  
22  
23  
24  
25  
26  
27  
28  
29  
30  
31  
32  
33  
34  
35  
36  
37  
38  
39  
40  
41  
42  
43

44 The experiments were conducted using micro-electro-mechanical heaters as sample  
45 support. A part of the experiments employed the Protochips Aduro system, which consists of  
46 silicon chips supporting silicon carbide membranes perforated with 7x7 holes near the center.<sup>47</sup>  
47 Prior to sample loading, chips were exposed to Ar/O<sub>2</sub> plasma for cleaning. In the experiment,  
48 sample dispersed on the membranes was heated by resistively passing an electrical current  
49  
50  
51  
52  
53  
54  
55  
56  
57  
58  
59  
60



1  
2  
3 through the membrane. The membrane current-temperature characteristic was calibrated using  
4  
5 pyrometry at a pressure of  $1.3 \times 10^{-2}$  mbar by the manufacturer (Protochips). During gas exposure  
6  
7 in the microscope, additional heat dissipation to the gas phase was accounted for by operating the  
8  
9 membrane in a constant resistance mode.<sup>37</sup> The other part of the experiments employed the FEI  
10  
11 Company NanoEx system, which consists of silicon chips with a silicon nitride membrane  
12  
13 perforated with 22 holes near its center and a conductive thin film with four electrodes for  
14  
15 resistive heating and on-board temperature sensing.<sup>45</sup> Prior to sample loading, chips were also  
16  
17 exposed to Ar/O<sub>2</sub> plasma for cleaning. The temperature-resistance characteristic of the chips was  
18  
19 provided by the manufacturer (FEI Company).  
20  
21  
22

23  
24 During a sulfidation experiment, 3-4 sample regions were monitored. The regions were  
25  
26 located at distances larger than the width of the electron beam, so that the regions were  
27  
28 monitored separately. As sulfidation of the sample progressed, each region was imaged every  
29  
30 approximately 15 min. and each imaging step lasted for a maximum of 60 s for positioning,  
31  
32 focusing and image acquisition. The total experiment duration was 240-300 min, corresponding  
33  
34 to a total of up to 21 electron beam exposures of each region. The maximal total accumulated  
35  
36 electron dose incident on a region in the *in situ* experiments was therefore  $189 \times 10^3 \text{ e}^-/\text{\AA}^2$ , using  
37  
38 an electron dose rate of  $150 \text{ e}^-/(\text{\AA}^2\text{s})$ . At each position and time step, an image series of 5 or 10  
39  
40 sequential images was acquired. These images were post-aligned using cross-correlation and  
41  
42 summed to the final displayed images with improved signal-to-noise-ratio. Immediately after an  
43  
44 imaging step, the electron beam was moved to the next sample position. This imaging strategy  
45  
46 was applied to minimize the total dose rate while maintaining a detectable image signal.<sup>48</sup>  
47  
48  
49 Additional images series were obtained after termination of the sulfidation reaction at positions  
50  
51  
52  
53  
54  
55  
56  
57  
58  
59  
60

1  
2  
3 without prior exposure to the electron beam (*post mortem*). These *post mortem* images were  
4  
5 acquired at a base vacuum below  $5 \times 10^{-6}$  mbar and 120°C.  
6  
7

8 The magnification of the TEM images was calibrated relative to a standard Au/C  
9  
10 calibration grid. The images are represented as a direct representation of the summed CCD  
11  
12 current outputs in a monochromatic green color scale with only a linear adjustment of the image  
13  
14 contrast and brightness.  
15  
16

17 **Image simulation.** High-resolution TEM images of MoO<sub>2</sub> were simulated using the multi-slice  
18  
19 approach as implemented in the MacTempasX software.<sup>49</sup> To describe the Philips CM300  
20  
21 microscope, the simulations employed an incident electron beam energy of 300 keV, spherical  
22  
23 aberration coefficient of  $C_s = 1.4$  mm, a convergence angle of 0.3 mrad, a defocus spread of 8.3  
24  
25 nm, an outer objective aperture of 0.14 nm, and a mechanical vibration amplitude in the imaging  
26  
27 plane of 0.07 nm. The MoO<sub>2</sub> nanoparticles were described by a monoclinic MoO<sub>2</sub> crystal  
28  
29 structure<sup>32</sup> belonging to the P2<sub>1</sub>/c space group.  
30  
31  
32

33 **Theoretical calculations.** The GPAW<sup>50,51</sup> density functional theory code was employed in finite  
34  
35 difference mode using a grid spacing of 0.18 Å to obtain total energies. The exchange and  
36  
37 correlation was described by the revised Perdew-Burke-Ernzerhof (RPBE) functional. All atomic  
38  
39 positions in the systems involving MoO<sub>2</sub> and MoS<sub>2</sub> structures were relaxed until the largest  
40  
41 interatomic force was smaller than or equal to 0.05 eV/Å and the molecules were relaxed to a  
42  
43 value less than 0.01 eV/Å. The DFT electronic energies of H<sub>2</sub>S and H<sub>2</sub>O were corrected with  
44  
45 zero-point energies and entropic contributions. The zero-point energy corrections were obtained  
46  
47 by performing vibrational analysis calculations in GPAW using the harmonic approximation.<sup>52</sup>  
48  
49 The remaining thermodynamic corrections were obtained from thermochemical tables.<sup>53</sup> The  
50  
51 calculations employed reaction conditions at 250°C with 0.1 mbar H<sub>2</sub>S and 0.9 mbar H<sub>2</sub>,  
52  
53  
54  
55  
56  
57  
58  
59  
60

1  
2  
3 matching the experimental sulfidation conditions. The calculations used an estimated H<sub>2</sub>O  
4  
5 pressure of 10<sup>-3</sup> mbar to reflect an upper limit of the residual gas phase in the electron  
6  
7 microscope.  
8  
9

10 The bulk structure of monoclinic MoO<sub>2</sub> was modeled using a unit cell consisting of 4 Mo  
11  
12 and 8 O atoms periodic in the x, y and z directions, respectively. Bulk MoS<sub>2</sub> was modeled as  
13  
14 infinite layers periodic in the x [110] and y [1-10] directions, separated by vacuum in the z [002]  
15  
16 direction and with 2 Mo and 4 S atoms in the unit cell. The Brillouin zone was sampled with  
17  
18 8,8,8 k-points in the x, y and z directions, respectively, both for bulk MoO<sub>2</sub> and MoS<sub>2</sub>. The  
19  
20 surfaces were modeled as symmetric layers of six (010) or (110) MoO<sub>2</sub> layers periodic in the x  
21  
22 [20-2] and y [101] or [-11-1] lattice directions and separated by 13 Å of vacuum in the z [010] or  
23  
24 [110] direction to prevent the surfaces from interacting due to the periodic boundary conditions.  
25  
26 The DFT calculations of the MoO<sub>2</sub> surface employed a periodicity of 4 along the [20-2]  
27  
28 direction. Importantly, the unit cell dimension of 4x a<sub>[20-2]</sub> is longer than the observed periodicity  
29  
30 of 3x a<sub>[20-2]</sub> at the MoO<sub>2</sub>:MoS<sub>2</sub> interface (Figure 3). The longer periodicity employed in the DFT  
31  
32 calculations ensured that periodic boundaries could be invoked and kept the computational time  
33  
34 low. Moreover, the periodicity in the DFT calculations is a pure geometric effect, because  
35  
36 identical exchange and Mo sublattice restructuring occurs locally in the larger cell and the extra  
37  
38 surface energy is canceled out by the reference (Figure 4a). Therefore, the present calculations  
39  
40 still capture the energetics in the transformation of three MoO<sub>2</sub> planes into one MoS<sub>2</sub> sheet.  
41  
42  
43  
44  
45

46 The Brillouin zone of the MoO<sub>2</sub> for the (010) and (110) surface slabs were sampled with  
47  
48 4, 4, 1 k-points in the x [20-2], y [101] or [-11-1] and z [010] or [110] directions, respectively.  
49  
50 The energies for the surface sulfidation were obtained by replacing all directly gas exposed O  
51  
52 atoms with S atoms and using gas phase H<sub>2</sub>O and H<sub>2</sub>S as references. For the calculations  
53  
54  
55  
56  
57  
58  
59  
60

1  
2  
3 regarding the reconstructive growth mechanism of MoS<sub>2</sub> the unit cell had to be repeated once in  
4 the x direction for the MoO<sub>2</sub> (010) and in the y direction for the MoO<sub>2</sub> (110) surface in order to  
5 prevent the formed MoS<sub>2</sub> sheets from overlapping. The Brillouin zone was thus sampled with 4,  
6 2, 1 k-points for the (010) system and 2, 4, 1 k-points for the (110) system in the x [20-2], y  
7 [101] or [-11-1] and z [010] or [110] directions, respectively. Details regarding calculation of the  
8 data points in Figure 4e are given in Supplementary methods in the Supporting Information.  
9  
10  
11  
12  
13  
14  
15  
16  
17  
18

### 19 **Acknowledgment.**

20  
21 The work was performed at the electron microscope facility at Haldor Topsoe A/S. CDP  
22 acknowledges financial support from Innovation Fund Denmark (grant Cat-C), and MS  
23 acknowledges financial support from Innovation Fund Denmark (grant HYDECAT). The authors  
24 acknowledge S. Ullmann (Haldor Topsoe A/S), S. Kegnæs (Technical University of Denmark  
25 (DTU)) and Q. Ramasse (SuperSTEM, UK) for fruitful discussions.  
26  
27  
28  
29  
30  
31  
32  
33  
34

### 35 **Supporting Information.**

36  
37 Note, Supplementary methods and Figures S1-S12 (PDF)

38  
39  
40 Video S1 accompanies Figure 2 and shows a MoO<sub>2</sub> nanocrystal during the exposure to 1 mbar of  
41 10% H<sub>2</sub>S in H<sub>2</sub> at 250°C. The images are recorded with 15 min intervals, with the first image  
42 equivalent to 45 min of gas exposure. The movie is displayed with 2 frames per second. Each  
43 frame corresponds to an image series of 5 exposures, which are post-aligned using cross-  
44 correlation and summed to improve the image signal-to-noise ratio. description (AVI)  
45  
46  
47  
48  
49  
50  
51  
52  
53  
54  
55  
56  
57  
58  
59  
60

## References

- 1 Tenne, R. Inorganic Nanotubes and Fullerene-like Nanoparticles. *Nat. Nanotechnol.* **2006**, 1, 103-111.
- 2 Xu, H.; Liu, S.; Ding, Z.; Tan, S. J. R.; Yam, K. M.; Bao, Y.; Nai, C. T.; Ng, M.-F.; Lu, J.; Zhang, C Loh, K. P. Oscillating Edge States in One-Dimensional MoS<sub>2</sub> Nanowires. *Nat. Commun.* **2016**, 7, 12904.
- 3 Bollinger, M. V.; Lauritsen, J. V.; Jacobsen, K. W.; Nørskov, J. K.; Helveg, S.; Besenbacher, F. One-Dimensional Metallic Edge States in MoS<sub>2</sub>. *Phys. Rev. Lett.* **2001**, 87, 196803.
- 4 Yin, X.; Ye, Z.; Chenet, D. A.; Ye, Y.; O'Brien, K.; Hone, J. C.; Zhang, X. Edge Nonlinear Optics on a MoS<sub>2</sub> Atomic Monolayer. *Science* **2014**, 344, 488-490.
- 5 Vojvodic, A.; Hinnemann, B.; Nørskov, J. K. Magnetic Edge States in MoS<sub>2</sub> Characterized by Density-Functional Theory. *Phys. Rev. B* **2009**, 80, 125416.
- 6 Chhowalla, M.; Shin, H. S.; Eda, G.; Li, L.-J.; Loh, K. P.; Zhang, H. The Chemistry of Two-Dimensional Layered Transition Metal Dichalcogenide Nanosheets. *Nat. Chem.* **2013**, 5, 263-275.
- 7 Deng, D.; Novoselov, K. S.; Fu, Q.; Zheng, N.; Tian, Z.; Bao, X. Catalysis with Two-Dimensional Materials and their Heterostructures. *Nat. Nanotechnol.* **2016**, 11, 218-230.
- 8 Prins, R. Energy-Related Catalysis: Hydrotreating Reactions: Hydrodesulfurization, Hydrodenitrogenation, Hydrodeoxygenation and Hydrodechlorination in *Handbook of Heterogeneous Catalysis* (eds. Ertl, G., Knözinger, H. & Weitkamp, J.), Wiley-VCH Verlag GmbH, 2008.
- 9 Besenbacher, F.; Brorson, M.; Clausen, B.S.; Helveg, S.; Hinnemann, B.; Kibsgaard, J.; Lauritsen, J.V.; Moses, P.G.; Nørskov, J.K.; Topsøe, H. Recent STM, DFT and HAADF-STEM Studies of Sulfide-Based Hydrotreating Catalysts: Insight into Mechanistic, Structural and Particle Size Effects. *Catal. Today* **2008**, 130, 86-96.

- 1  
2  
3 10 Jaramillo, T.F.; Jørgensen, K.P.; Bonde, J.; Nielsen, J.H.; Horch, S.; Chorkendorff, I.  
4 identification of Active Edge Sites for Electrochemical H<sub>2</sub> Evolution from MoS<sub>2</sub>  
5 Nanocatalysts. *Science* **2007**, 317, 100-102.  
6  
7  
8 11 Hou, Y.; Abrams, B. L.; Vesborg, P. C. K.; Björketun, M. E.; Herbst, K.; Bech, L.; Setti,  
9 A. M.; Damsgaard, C. D.; Pedersen, T.; Hansen, O.; Rossmeisl, J.; Dahl, S.; Nørskov, J.  
10 K.; Chorkendorff, I. Bioinspired Molecular Co-Catalysts Bonded to a Silicon  
11 Photocathode for Solar Hydrogen Evolution. *Nat. Mater.* **2011**, 10, 434-438.  
12  
13 12 Asadi, M.; Kumar, B.; Behranginia, A.; Rosen, B. A.; Baskin, A.; Repnin, N.; Pisasale,  
14 D.; Phillips, P.; Zhu, W.; Haasch, R.; Klie, R. F.; Král, P.; Abiade, J.; Salehi-Khojin, A.  
15 Robust Carbon Dioxide Reduction on Molybdenum Disulphide Edges. *Nat Commun.*  
16 **2014**, 5, 4470.  
17  
18 13 Liu, C.; Kong, D.; Hsu, P.-C.; Yuan, H.; Lee, H.-W.; Liu, Y.; Wang, H.; Wang, S.; Yan,  
19 K.; Lin, D.; Maraccini, P. A.; Parker, K. M.; Boehm, A. B.; Cui, Y. Rapid Water  
20 Disinfection using Vertically Aligned MoS<sub>2</sub> Nanofilms and Visible Light. *Nat.*  
21 *Nanotechnol.* **2016**, 11, 1098-1104.  
22  
23 14 Tuxen, A. K.; Füchtbauer, H. G.; Temel, B.; Hinnemann, B.; Topsøe, H.; Knudsen, K.  
24 G.; Besenbacher, F.; Lauritsen, J. V. Atomic-Scale Insight into Adsorption of Sterically  
25 Hindered Dibenzothiophenes on MoS<sub>2</sub> and Co–Mo–S Hydrotreating Catalysts. *J. Catal.*  
26 **2012**, 295, 146-154.  
27  
28 15 Hayden, T. F.; Dumesic, J. A. Studies of the Structure of Molybdenum Oxide and Sulfide  
29 Supported on Thin Films of Alumina. *J. Catal.* **1987**, 103, 366-384.  
30  
31 16 Sakashita, Y.; Araki, Y.; Honna, K.; Shimada, H. Orientation and Morphology of  
32 Molybdenum Sulfide Catalysts Supported on Titania Particles, Observed by using High-  
33 Resolution Electron Microscopy. *Appl. Catal., A* **2000**, 197, 247-253.  
34  
35 17 Shimada, H. Morphology and Orientation of MoS<sub>2</sub> Clusters on Al<sub>2</sub>O<sub>3</sub> and TiO<sub>2</sub> Supports  
36 and their Effect on Catalytic Performance. *Catal. Today* **2003**, 86, 17-29.  
37  
38 18 Kibsgaard, J.; Chen, Z. B.; Reinecke, B. N.; Jaramillo, T. F. Engineering the Surface  
39 Structure of MoS<sub>2</sub> to Preferentially Expose Active Edge Sites for Electrocatalysis. *Nat.*  
40 *Mater.* **2012**, 11, 963-969.  
41  
42 19 Kong, D.; Wang, H.; Cha, J. J.; Pasta, M.; Koski, K. J.; Yao, J.; Cui, Y. Synthesis of  
43 MoS<sub>2</sub> and MoSe<sub>2</sub> Films with Vertically Aligned Layers. *Nano Lett.* **2013**, 13, 1341-1347.  
44  
45  
46  
47  
48  
49  
50  
51  
52  
53  
54  
55  
56  
57  
58  
59  
60

- 1  
2  
3 20 Wang, H.; Kong, D.; Johanes, P.; Cha, J. J.; Zheng, G.; Yan, K.; LiU, N.; Cui, Y. MoSe<sub>2</sub>  
4 and WSe<sub>2</sub> Nanofilms with Vertically Aligned Molecular Layers on Curved and Rough  
5 Surfaces. *Nano Lett.* **2013**, 13, 3426-3433.  
6  
7  
8 21 Jung, Y.; Shen, J.; Liu, Y.; Woods, J. M.; Sun, Y.; Cha, J. J. Metal Seed Layer  
9 Thickness-Induced Transition from Vertical to Horizontal Growth of MoS<sub>2</sub> and WS<sub>2</sub>.  
10 *Nano Lett.* **2014**, 14, 6842-6849.  
11  
12  
13 22 Wang, H.; Tsai, C.; Kong, D.; Chan, K.; Abild-Pedersen, F.; Nørskov, J. K.; Cui, Y.  
14 Transition-Metal Doped Edge Sites in Vertically Aligned MoS<sub>2</sub> Catalysts for Enhanced  
15 Hydrogen Evolution. *Nano Res.* **2015**, 8, 566-575.  
16  
17  
18 23 Fei, L.; Lei, S.; Zhang, W.-B.; Lu, W.; Lin, Z.; Lam, C. H.; Chai, Y.; Wang, Y. Direct  
19 TEM Observations of Growth Mechanisms of Two-Dimensional MoS<sub>2</sub> Flakes. *Nat.*  
20 *Commun.* **2016**, 7, 12206.  
21  
22  
23 24 Deng, Z. H.; Li, L.; Ding, W.; Xiong, K.; Wei, Z. D. Synthesized Ultrathin MoS<sub>2</sub>  
24 Nanosheets Perpendicular to Graphene for Catalysis of Hydrogen Evolution Reaction.  
25 *ChemComm* **2015**, 51, 1893-1896.  
26  
27  
28 25 Lan, F.; Lai, Z.; Xu, Y.; Cheng, H.; Wang, Z.; Qi, C.; Chen, J.; Zhang, S. Synthesis of  
29 Vertically Standing MoS<sub>2</sub> Triangles on SiC. *Sci. Rep.* **2016**, 6, 31980.  
30  
31  
32 26 Li, S.; Wang, S.; Salamone, M. M.; Robertson, A. W.; Nayak, S.; Kim, H.; Tsang, S. C.  
33 E.; Pasta, M.; Warner, J. H. Edge-Enriched 2D MoS<sub>2</sub> Thin Films Grown by Chemical  
34 Vapor Deposition for Enhanced Catalytic Performance. *ACS Catal.* **2017**, 7, 877-886.  
35  
36  
37 27 Arrouvel, C.; Breysse, M.; Toulhoat, H.; Raybaud, P. A Density Functional Theory  
38 Comparison of Anatase (TiO<sub>2</sub>)- and  $\gamma$ -Al<sub>2</sub>O<sub>3</sub>-Supported MoS<sub>2</sub> Catalysts. *J. Catal.* **2005**,  
39 232, 161-178.  
40  
41  
42 28 Costa, D.; Arrouvel, C.; Breysse, M.; Toulhoat, H.; Raybaud, P. Edge Wetting Effects of  
43  $\gamma$ -Al<sub>2</sub>O<sub>3</sub> and Anatase-TiO<sub>2</sub> Supports by MoS<sub>2</sub> and CoMoS Active Phases: A DFT Study.  
44 *J. Catal.* **2007**, 246, 325-343.  
45  
46  
47 29 Helveg, S. An Industrial Perspective of the Impact of Haldor Topsøe on (*In Situ*) Electron  
48 Microscopy in Catalysis. *J. Catal.* **2015**, 328, 102-110.  
49  
50  
51 30 Tao, F.; Crozier, P. A. Atomic-Scale Observations of Catalyst Structures under Reaction  
52 Conditions and during Catalysis. *Chem. Rev.* **2016**, 116, 3487-3539.  
53  
54  
55  
56  
57  
58  
59  
60

- 1  
2  
3 31 Ross, F. M. Opportunities and Challenges in Liquid Cell Electron Microscopy. *Science*  
4 **2015**, 350, aaa9886.  
5  
6 32 Feldman, Y.; Wasserman, E.; Srolovitz, D. J.; Tenne, R. High-Rate, Gas-Phase Growth  
7 of MoS<sub>2</sub> Nested Inorganic Fullerenes and Nanotubes. *Science* **1995**, 267, 222-225.  
8  
9 33 Feldman, Y.; Frey, G. L.; Homyonfer, M.; Lyakhovitskaya, V.; Margulis, L.; Cohen, H.;  
10 Hodes, G.; Hutchison, J. L.; Tenne, R. Bulk Synthesis of Inorganic Fullerene-Like MS<sub>2</sub>  
11 (M = Mo, W) from the Respective Trioxides and the Reaction Mechanism. *J. Am. Chem.*  
12 *Soc.* **1996**, 118, 5362–5367.  
13  
14 34 Brandt, B. G.; Skapski, A. C. A Refinement of the Crystal Structure of Molybdenum  
15 Dioxide. *Acta Chem. Scand.* **1967**, 21, 661-672.  
16  
17 35 Wienold, J.; Jentoft, R. E.; Ressler, T. Structural Investigation of the Thermal  
18 Decomposition of Ammonium Heptamolybdate by *In Situ* XAFS and XRD. *Eur. J.*  
19 *Inorg. Chem.* **2003**, 2003, 1058-1071.  
20  
21 36 Stockmann, R. M.; Zandbergen, H. V.; Langeveld, A. D. v.; Moulijn, J. A. Investigation  
22 of MoS<sub>2</sub> on  $\gamma$ -Al<sub>2</sub>O<sub>3</sub> by HREM with Atomic Resolution. *J. Mol. Catal. A: Chem.* **1995**,  
23 102, 147–161.  
24  
25 37 Hansen, L. P.; Johnson, E.; Brorson, M.; Helveg, S. Growth Mechanism for Single- and  
26 Multi-Layer MoS<sub>2</sub> Nanocrystals. *J. Phys. Chem. C* **2014**, 118, 22768-22773.  
27  
28 38 Margulis, L.; Salitra, G.; Tenne, R.; Talianker, M. Nested Fullerene-Like Structures.  
29 *Nature* **1993**, 365, 113-114.  
30  
31 39 Shannon, R. D.; Rossi, R. C. Definition of Topotaxy. *Nature* **1964**, 202, 1000-1001.  
32  
33 40 Muijsers, J. C.; Weber, T.; Vanhardeveld, R. M.; Zandbergen, H. W.; Niemantsverdriet,  
34 J. W. Sulfidation Study of Molybdenum Oxide Using MoO<sub>3</sub>/SiO<sub>2</sub>/Si(100) Model  
35 Catalysts and Mo-<sup>IV</sup><sub>3</sub>-Sulfur Cluster Compounds. *J. Catal.* **1995**, 157, 698-705.  
36  
37 41 Weber, T.; Muijsers, J. C.; van Wolput, J. H. M. C. ; Verhagen, C. P. J.;  
38 Niemantsverdriet, J. W. Basic Reaction Steps in the Sulfidation of Crystalline MoO<sub>3</sub> to  
39 MoS<sub>2</sub>, As Studied by X-ray Photoelectron and Infrared Emission Spectroscopy. *J. Phys.*  
40 *Chem.* **1996**, 100, 14144–14150.  
41  
42 42 Tauster, S. J.; Pecoraro, T. A.; Chianelli, R. R. Structure and Properties of Molybdenum  
43 Sulfide: Correlation of O<sub>2</sub> Chemisorption with Hydrodesulfurization Activity, *J. Catal.*  
44 **1980**, 63, 515-519.  
45  
46  
47  
48  
49  
50  
51  
52  
53  
54  
55  
56  
57  
58  
59  
60



- 1  
2  
3 43 Shi, Q.; Li, Y.; Zhou, Y.; Miao, S.; Ta, N.; Zhan, E.; Liu, J.; Shen, W. The Shape Effect  
4 of TiO<sub>2</sub> in Vox/TiO<sub>2</sub> Catalysts for Selective Reduction of NO by NH<sub>3</sub>. *J. Mater. Chem. A*  
5 **2015**, 27, 14409-14415.  
6  
7  
8 44 Picher, M.; Mazzucco, S.; Blankenship, S.; Sharma, R. Vibrational and Optical  
9 Spectroscopies Integrated with Environmental Transmission Electron Microscopy.  
10 *Ultramicroscopy* **2015**, 150, 10-15.  
11  
12  
13 45 Mele, L.; Konings, S.; Dona, P.; Evertz, F.; Mitterbauer, C.; Faber, P.; Schampers, R.;  
14 Jinschek, J. R. MEMS-Based Heating Holder for the Direct Imaging of Simultaneous *In*  
15 *Situ* Heating and Biasing Experiments in Scanning/Transmission Electron Microscopes.  
16 *Microsc. Res. Tech.* **2016**, 79, 239-250.  
17  
18  
19  
20 46 Hansen, P. L.; Helveg, S.; Datye, A. K. Atomic-Scale Imaging of Supported Metal  
21 Nanocluster Catalysts in the Working State. *Adv. Catal.* **2006**, 50, 77-95.  
22  
23  
24 47 Allard, L. F.; Bigelow, W. C.; Jose-Yacamán, M.; Nackashi, D. P.; Damiano, J.; Mick, S.  
25 E. New MEMS-Based System for Ultra-High-Resolution Imaging at Elevated  
26 Temperatures. *Microsc. Res. Tech.* **2009**, 79, 208-215.  
27  
28  
29 48 Helveg, S.; Kisielowski, C. F.; Jinschek, J. R.; Specht, P.; Yuan, G.; Frei, H. Observing  
30 Gas-Catalyst Dynamics at Atomic Resolution and Single-Atom Sensitivity. *Micron* **2015**,  
31 68, 176-185.  
32  
33  
34 49 Kilaas, R. *Total Resolution LLC: Software for High Resolution Electron Microscopy*,  
35 <<http://www.totalresolution.com>> (2016).  
36  
37  
38 50 Mortensen, J. J.; Hansen, L. B.; Jacobsen, K. W. Real-Space Grid Implementation of the  
39 Projector Augmented Wave Method. *Phys. Rev. B* **2005**, 71, 035109.  
40  
41 51 Enkovaara, J.; Rostgaard, C.; Mortensen, J. J.; Chen, J.; Dulak, M.; Ferrighi, L.; Gavnholt,  
42 J.; Glinsvad, C.; Haikola, V.; Hansen, H. A. *et al.* Electronic Structure Calculations with  
43 GPAW: A Real-Space Implementation of the Projector Augmented-Wave Method. *J.*  
44 *Phys.: Condens. Matter* **2010**, 22, 253202.  
45  
46  
47  
48 52 Bahn, S. R.; Jacobsen, K. W. An Object-Oriented Scripting Interface to a Legacy  
49 Electronic Structure Code. *Comput. Sci. Eng.* **2002**, 4, 56-66.  
50  
51 53 Chase, M. W. *NIST-JANAF Thermochemical Tables*. 4 edn, (American Chemical  
52 Society, 1998).  
53  
54  
55  
56  
57  
58  
59  
60

1  
2  
3  
4  
5  
6  
7 **Figure 1.** Surface sulfidation of MoO<sub>2</sub> nanocrystals. **a** An illustration of a MoO<sub>2</sub> nanocrystal  
8 before and after partial sulfidation by heating in H<sub>2</sub>S/H<sub>2</sub>. In the sulfided state, a partial coverage  
9 of co-existing *e*-MoS<sub>2</sub> and *p*-MoS<sub>2</sub> phases is illustrated by the MoS<sub>2</sub> sheets (yellow) orientated  
10 perpendicular to and along the MoO<sub>2</sub> crystal facets (blue), respectively. **b, c** TEM images of  
11 MoO<sub>2</sub> nanocrystals after exposure to 10% H<sub>2</sub>S in H<sub>2</sub> *in situ* at (b) 250°C for 300 min and (c)  
12 300°C for 240 min. The images are acquired in the microscope base vacuum ( $5 \times 10^{-6}$  mbar) at  
13 120°C. A distinct lattice constant with the MoS<sub>2</sub> (002) lattice spacing of 0.62nm and the MoS<sub>2</sub>  
14 (100) lattice spacing of 0.27 nm are resolved at the surface of the MoO<sub>2</sub> nanocrystals in b and c.  
15 Crystal lattice planes with spacing corresponding to MoO<sub>2</sub> are resolved in the bulk of the  
16 nanoparticles.  
17  
18  
19  
20  
21  
22  
23  
24  
25  
26  
27  
28  
29  
30  
31  
32

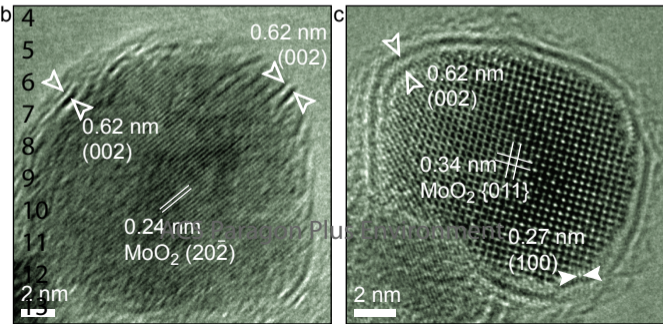
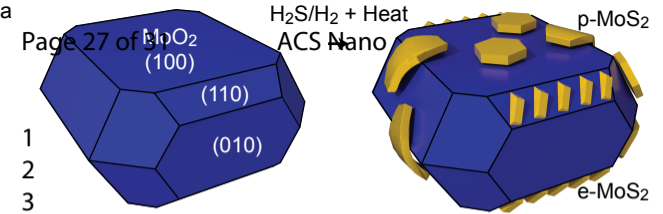
33 **Figure 2.** Time-resolved TEM imaging of a MoO<sub>2</sub> nanocrystal *in situ* during sulfidation. **a-f**  
34 Time-resolved TEM of a MoO<sub>2</sub> nanocrystal during the exposure to 1 mbar of 10% H<sub>2</sub>S in H<sub>2</sub> at  
35 250°C. The images are extracted from Video S1 in the Supporting Information at times [and  
36 accumulated electron dose] of (a) 45 min [ $9 \times 10^3$  e<sup>-</sup>/Å<sup>2</sup>], (b) 65 min [ $27 \times 10^3$  e<sup>-</sup>/Å<sup>2</sup>], (c) 85 min  
37 [ $45 \times 10^3$  e<sup>-</sup>/Å<sup>2</sup>], (d) 160 min [ $81 \times 10^3$  e<sup>-</sup>/Å<sup>2</sup>], (e) 220 min [ $126 \times 10^3$  e<sup>-</sup>/Å<sup>2</sup>] and (f) 280 min  
38 [ $153 \times 10^3$  e<sup>-</sup>/Å<sup>2</sup>]. The time of 0 min corresponds to the time of gas introduction in the experiment.  
39 The inserts show Fast Fourier Transforms of the corresponding images. The open arrowhead  
40 indicates the location of *e*-MoS<sub>2</sub>. First the MoO<sub>2</sub> (01-1) and later the (20-2) lattice planes are  
41 visible in the MoO<sub>2</sub> bulk due to slight rotation of the nanocrystal with time. All TEM images  
42 have the same size.  
43  
44  
45  
46  
47  
48  
49  
50  
51  
52  
53  
54  
55  
56  
57  
58  
59  
60

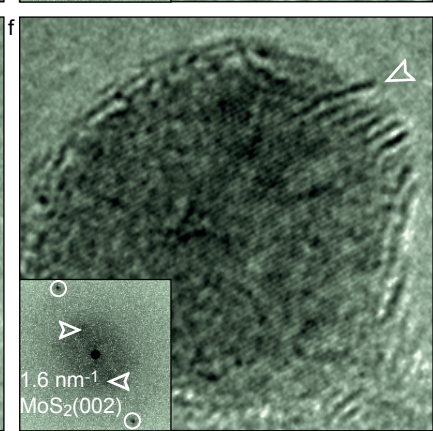
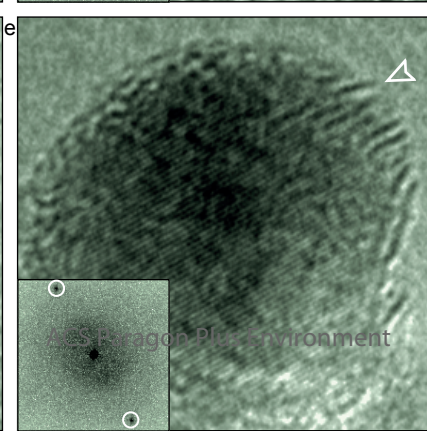
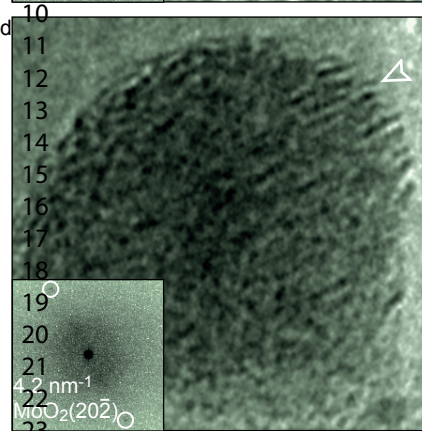
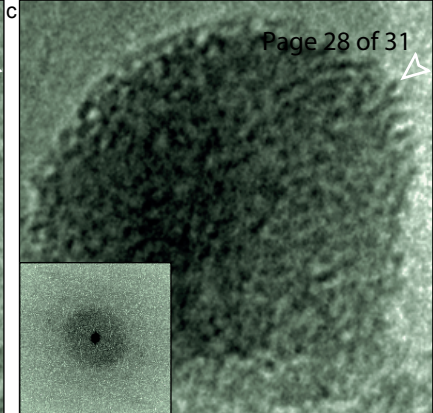
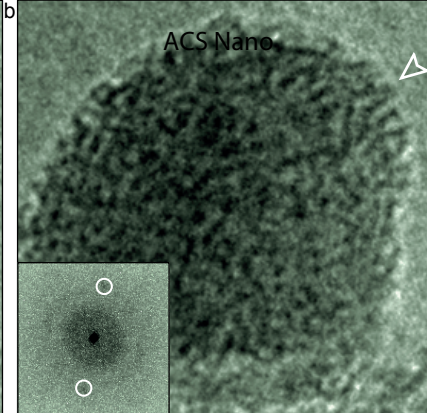
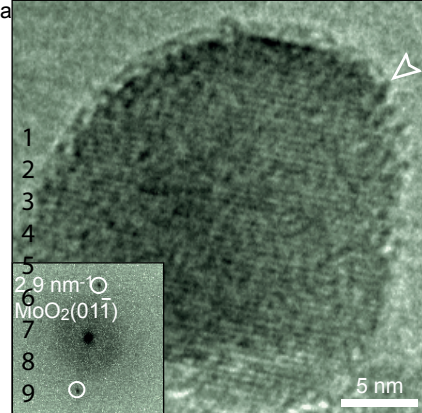
1  
2  
3  
4  
5  
6  
7  
8 **Figure 3.** Interface between *e*-MoS<sub>2</sub> and MoO<sub>2</sub>. **a** Close-up high resolution TEM image of the  
9 nanocrystal in Figure 2, acquired *post mortem* after sulfidation for 300 min exposure to 1 mbar  
10 10% H<sub>2</sub>S in H<sub>2</sub> at 250°C. The superimposed crystal lattice vectors and zone axis (Z.A.)  
11 correspond to MoO<sub>2</sub>. **b** FFT image revealing the MoO<sub>2</sub> (20-2), MoO<sub>2</sub> (11-1) and MoS<sub>2</sub> (002)  
12 lattice planes, corresponding to a zone axis (Z.A.) view of the MoO<sub>2</sub> nanocrystal in the [101]  
13 direction. **c** Image intensity line-scans in MoO<sub>2</sub> and *e*-MoS<sub>2</sub> obtained along MoO<sub>2</sub>[20-2] and  
14 averaged over 10 pixels corresponding to the blue (MoO<sub>2</sub>), orange (*e*-MoS<sub>2</sub>) and yellow (*e*-  
15 MoS<sub>2</sub>) boxes in (a).  
16  
17  
18  
19  
20  
21  
22  
23  
24  
25  
26  
27

28 **Figure 4.** Atomic mechanism for topotaxy of *e*-MoS<sub>2</sub> at the MoO<sub>2</sub>(110) surface. **a-d** The  
29 topotactic transformation is illustrated by ball models of the atomic structures at an inclined  
30 projection (left) and by sketches of the [-11-1] oriented atomic rows with Mo in the center and  
31 the anionic content as the rim (right). The colors coding is dark blue for Mo in [-11-1] rows with  
32 the bulk density (full row), light blue for Mo in [-11-1] rows with half the bulk density (half  
33 row), red for O and yellow for S. Crystal directions are quoted with reference to the MoO<sub>2</sub>  
34 lattice. The atomic row numbering is equivalent in the ball models and sketches. All surface  
35 structures are obtained by DFT calculations. **a** Initial state for the sulfided MoO<sub>2</sub>(110) surface  
36 (indicated by the dashed line). **b** The sulfided MoO<sub>2</sub>(110) surface after displacement of row 1. **c**  
37 The sulfided MoO<sub>2</sub>(110) surface in (b) after displacement of row 3 and surface O-S exchange of  
38 the exposed oxide surface in rows 2, 4 and 5, resulting in a two-row *e*-MoS<sub>2</sub> sheet. **d** The  
39 sulfided MoO<sub>2</sub>(110) surface in (c) after displacement row 4 and 5 and O-S exchange in the  
40  
41  
42  
43  
44  
45  
46  
47  
48  
49  
50  
51  
52  
53  
54  
55  
56  
57  
58  
59  
60

1  
2  
3 exposed oxide surface, resulting in a four-row *e*-MoS<sub>2</sub> sheet aligned with the MoO<sub>2</sub>(20-2) planes.  
4

5 **e** Calculated Gibbs free energies per unit cell for (a-d) for both the MoO<sub>2</sub>(110) and (010)  
6  
7 surfaces (Methods).  
8  
9  
10  
11  
12  
13  
14  
15  
16  
17  
18  
19  
20  
21  
22  
23  
24  
25  
26  
27  
28  
29  
30  
31  
32  
33  
34  
35  
36  
37  
38  
39  
40  
41  
42  
43  
44  
45  
46  
47  
48  
49  
50  
51  
52  
53  
54  
55  
56  
57  
58  
59  
60

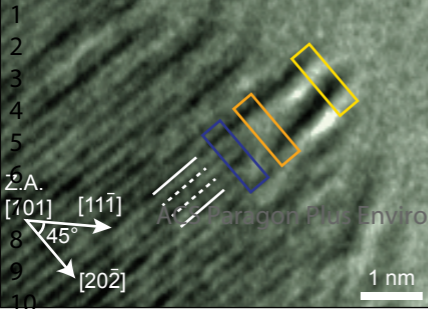




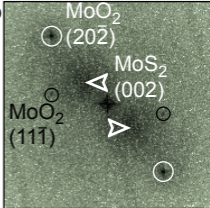
a

Page 29 of 31

ACS Nano



b



c

